Geophys. J. Int. (2003) **142,** 000–000

A Physical Model for Strain Accumulation in the San Francisco Bay Region

F.F. Pollitz and M. Nyst

U.S. Geological Survey, 345 Middlefield Rd. MS 977, Menlo Park, CA 94025 USA

Received —-; in original form —-

SUMMARY

Strain accumulation in tectonically active regions is generally a superposition of the effects of background tectonic loading, steady-state dislocation processes such as creep, and transient deformation. In the San Francisco Bay Region (SFBR), the most uncertain of these processes is transient deformation, which arises primarily in association with large historic earthquakes. As such it depends upon the history of faulting and the rheology of the crust and mantle, which together determine the pattern of longer-term (decade-scale) postseismic response to earthquakes. We utilize a set of 102 GPS velocity vectors in the SFBR in order to characterize the strain rate field and construct a physical model of its present deformation. We first perform an inversion for the continuous velocity gradient field from the discrete GPS velocity field, from which both tensor strain rate and rotation rate may be extracted. The present strain rate pattern is well-described as a nearly uniform shear strain rate oriented approximately $\mathrm{N}34^\circ\mathrm{W}$ (140 nanostrain/yr) plus a $\mathrm{N}56^\circ\mathrm{E}$ uniaxial compression rate averaging 20 nanostrain/yr across the shear zone. We fit the velocity and strain rate fields to a model of time-dependent deformation within a 135 km-wide, arcuate shear zone bounded by strong Pacific plate and Sierra Nevada block lithosphere to the SW and NE, respectively. Driving forces are purely lateral, consisting of shear zone deformation imposed by the relative motions between the thick Pacific plate and Sierra Nevada block lithospheres. Assuming a depth-dependent viscoelastic structure within the shear zone, we account for the effects of steady creep on faults and viscoelastic relaxation following the 1906 San Francisco and 1989 Loma Prieta earthquakes, subject to constant velocity boundary conditions on the edges of the shear zone. Fault creep is realized by evaluating dislocations on the creeping portions of faults in the fluid limit of the viscoelastic model. A priori fault-parallel motion is set to 38 mm/yr. A grid search based on fitting the observed strain rate pattern yields a mantle viscosity of 1.2×10^{19} Pa s and a fault-perpendicular convergence rate of ~ 3 mm/yr. Most of this convergence appears to be uniformly distributed in the Pacific-Sierra Nevada plate boundary zone.

Key words: crustal deformation - strain accumulation - San Francisco Bay.

1 INTRODUCTION

The San Francisco Bay Region (SFBR) is an active zone of strain accumulation accommodating about 37 - 40 mm/yr relative plate motion (Savage et al. 1998; Argus and Gordon 2001; Murray and Segall 2001; Prescott et al. 2001). Located within the Pacific - Sierra Nevada/Great Valley (SNGV) plate boundary zone, it is traversed by several major fault zones (figure 1) accommodating long term slip rates ranging from a few mm/yr for faults in the East Bay to as much as 25 mm/yr along the San Andreas fault (WG99 1999). Although historical observations of seismicity do not span even one San Andreas fault recurrence time, seismicity patterns indicate that the rate of moment release along the major faults is roughly in accord with the long term slip rates (Bakun 1999). Strain accumulation as measured by geodetic measurements is dominated by (fault-parallel) right-lateral shear on roughly N32°W trending strike-slip faults and an integrated fault-perpendicular relative motion about 2 - 3 mm/yr accommodated within the Pacific - SNGV plate boundary zone. Outstanding questions concerning the active deformation of this region are: (1) Is strain accumulation in the fault-parallel and fault-perpendicular senses uniform throughout the area or laterally variable? (2) Is strain accumulation temporally uniform or are transient strain processes contributing to present or past deformation? (3) What are the physical mechanisms that control strain accumulation? We shall address these questions by constructing a physical model of strain accumulation for the SFBR that is consistent with the present-day velocity field and allows a simple interpretation in terms of the geometry of the driving Pacific - SNGV relative tectonic motion. Unlike earlier interpretations of SFBR geodetic data, the proposed model does not depend explicitly on either the long term slip rates or locking depths associated with the faults. The new approach is motivated by a few observations. First, the strain accu-

mulation pattern may be explained to first order by simple shear across a $\sim$ 135 km wide shear zone (Savage et al. 1998). Second, present strain rate within 20 - 30 km of the San Andreas fault accounts for about 60% of the net plate-boundary strain (Savage et al. 1998; Murray and Segall 2001; Prescott et al. 2001), and strain rates are similarly elevated near the southern Santa Cruz mountains (Segall et al. 2000). Previous authors have documented that postseismic relaxation following the M7.8 1906 San Francisco earthquake and M6.9 Loma Prieta earthquakes may have led to localized elevated strain accumulation in the respective source regions for years or decades following the events (Thatcher 1983; Pollitz et al. 1998; Kenner and Segall 1999; Parsons 2002). If transient strain from each of these events persists today, then it may provide an explanation for the aforementioned observations of elevated strain rates.

In the following sections, we examine the deformation pattern in greater detail by deriving the regional strain rate field, describe the elements of our strain accumulation model, and discuss how the overall deformation pattern is shaped by the various contributing physical processes.

2 REGIONAL DEFORMATION

2.1 Velocity field

The GPS velocity field for the period 1994 to 2000 is shown in figure 2. It contains velocity vectors from 102 sites measured by the U.S. Geological Survey (USGS), Bay Area Regional Deformation Network (BARD), continuously Operating Reference Stations (CORS), and the International GPS Service (IGS). Details of the data processing may be found in Prescott et al. (2001) and Savage et al. (2003). The velocity field is an ensemble of six velocity profiles which traverse the SFBR. Plots of velocity along each individual profile are presented in figure 3. In these plots fault-parallel and fault-perpendicular velocities are resolved along directions N33.85°W and N56.15°E, respectively for profiles 1, 2 and 3, and N40°W and N50°E, respectively for profiles 4, 5 and 6. These are averages of the local direction of Pacific - SNGV motion at the latitude of San Francisco. The observed velocity field exhibits predominantly simple shear within a $\sim$ 135 km wide plate boundary zone, offsets across creeping segments of the San Andreas Fault (SAF) system, and, where it exists, distributed fault-perpendicular contraction. The effects of fault creep are most evident along profiles 5 and 6. Profiles 5 and 6 each show large offsets along the Calaveras fault, and Profile 6 shows a large offset across the SAF as well.

2.2 Velocity gradient field

The velocity field is useful for examining background tectonic motions, but suspected processes such as postseismic relaxation and regional contraction are more subtle and smaller scale features that are better exhibited in the strain rate field. In order to extract information from the velocity field that is not directly evident in either the velocity vectors or the profiles, we construct an image of the regional strain and rotation rate fields. This is done by fitting the velocity field to a velocity gradient field subject to smoothing constraints in a damped least-squares inversion procedure (Spakman and Nyst 2002). In this method one converts the velocity field into a spatially continuous velocity gradient field in coherent crustal blocks and spatially discontinuous motion on boundaries between the blocks. The continuous velocity gradient field may be interpreted in terms of tectonic loading and postseismic relaxation. The discontinuous velocity gradient field is attributable to either coseismic offsets during the period of observation or fault creep.

We parameterize the study region by constructing a triangulation grid of uniform density. The size of the Delaunay triangles is chosen small enough to adequately interpolate between the GPS stations and represent possible small scale variations in the strain rate field. We compute the 4 components of the horizontal velocity gradient tensor ($\boldsymbol{\nabla v}$) at each node and adopt a linear dependence between the vertices of each triangle. To ensure that creep is not mapped into the continuous velocity gradient field we parameterize the principle creeping sections (figures 2 and 11E) as discontinuities in the triangular grid and assume that the velocity gradient field is piece-wise continuous. We impose a-priori the creep profile that is described in more detail in section 4.

In addition to the GPS data we impose an extra constraint that requires $\boldsymbol{\nabla} \times \boldsymbol{\nabla v} = \mathbf{0}$ within each triangle, based on the zero-curl property of a continuous gradient vector field (Spakman and Nyst 2002). The inversion procedure selects a solution that fits the data in a least squares sense and at the same time minimizes the model norm:

$$\boldsymbol{m} = (\boldsymbol{A}^T \boldsymbol{C}_d^{-1} \boldsymbol{A} + \alpha_d^2 \boldsymbol{I} + \alpha_s \boldsymbol{D}^T \boldsymbol{D})^{-1} \boldsymbol{A}^T \boldsymbol{C}_d^{-1} \boldsymbol{d} \quad (1)$$

where $\boldsymbol{m}$ is the model parameter vector, $\boldsymbol{A}$ contains the components that link velocity to the velocity gradient and $\boldsymbol{C}_d$ is the data covariance matrix with 1-σ uncertainties of the horizontal GPS velocity components and their correlation coefficients. The trade-off between good data fit and minimal model norm can be regulated by tuning three parameters: α_d and α_s control the influence of amplitude damping ($\boldsymbol{I}$) and smoothing ($\boldsymbol{D}$), respectively, and γ_r determines the weight on the $\boldsymbol{\nabla} \times \boldsymbol{\nabla v} = \mathbf{0}$ constraints (hereafter *extra data* constraints). Since the extra data constraints are treated as data we weigh them by tuning their error ($\sim 1/\gamma_r$) in the data covariance matrix $\boldsymbol{C}_d$. A small error (equivalent to a large γ_r) increases the influence of the extra data constraints with respect to the GPS velocity data. In the inversion procedure the full model covariance ($\boldsymbol{C}$) and resolution ($\boldsymbol{R}$) matrices are computed.

For the selection of the final solution we consider fits of GPS velocity data and extra data constraints and the quality of model covariance and model resolution. For the model covariance we compute the size of the unit model covariance matrix as a measure for the amount of error amplification mapped from data to solution (Menke 1989, p. 67-68):

$$size[\boldsymbol{C}] = \sum_{i=1}^{M} C_{ii} \quad (2)$$

with M the number of model parameters. For the model resolution we compute the size of the resolution spread function to provide some average measure for the independence of the model parameters (Michelini and McEvilly 1991; Eberhart-Phillips and Reyners 1997):

$$size[\boldsymbol{S}] = \sum_{j=1}^{M} [S_j] = \sum_{j=1}^{M} log \left[|R_j|^{-1} \sum_{k=1}^{M} \left[\frac{R_{kj}}{|R_j|} \right]^2 D_{jk} \right]. \quad (3)$$

R_j stands for the j-th component of the diagonal of $\boldsymbol{R}$. R_{kj} represents all elements of the corresponding j-th row of $\boldsymbol{R}$, weighted by the distance D_{jk} between the nodes of the k-th and j-th model parameters. If S_j is relatively large then model parameter j is poorly resolved. This may be due to either a small diagonal resolution

value R_j or a strong dependence on other model parameters k, amplified with distance, or a combination of both.

Figures 4A and B display the well-known trade-off between resolution and model variance for different combinations of α_s and α_d (for constant γ_r). Two additional trading-off relations exist between resolution and data fit and between model variance and data fit, both as functions of γ_r (for constant α_s and α_d). An increase of the influence of the extra data constraints for constant α_s and α_d reduces the size of the spread function and increases data misfit. The coupling of the standard deviation of the extra data constraints to the inverse of γ_r causes the misfit of the extra constraints to grow with increasing γ_r. The final solution used for further interpretation has $size[\boldsymbol{S}] = 1245$, $size[\boldsymbol{C}] = 3.3 \cdot 10^{-5}/yr$, root mean square misfits of 1.5 for the GPS data and of 1.6 for the extra data constraints and is indicated by the white dot in figures 4.

Reasonably well resolved model parameters have a spread function value between 2 and 6 (figure 5C) with a diagonal resolution between 0.2 and 0.4 (or between 20% and 40%, figure 5A and B). For poorly resolved model parameters the spread function value is greater than 6. The interior of the study area, despite some localized areas with zero diagonal resolution, is relatively well resolved. As may be expected the areas with few or no stations are poorly resolved, i.e., north and east of San Pablo Bay and south and east of Monterey Bay (figure 5A). In general, the final solution has relatively small 1-σ model errors (figure 5D).

The piece-wise continuous velocity gradient field derived from the SFBR velocity field is shown in figures 6A, B and C. The pattern of the second invariant of the strain rate tensor (i.e., pure shear strain rate, figure 6A) combined with rotation rate (figure 6C) confirms that the regional deformation is dominated by right-lateral simple shear strain rate. It further reveals that somewhat greater strain accumulation is localized near the San Andreas Fault than around the East Bay faults (Hayward and Rodgers Creek faults; Greenville fault). The pattern of the first invariant of the strain rate tensor (i.e., areal strain rate, figure 6B) confirms an overall small regional contraction as noted by previous authors (Prescott et al. 2001; Murray and Segall 2001; Argus and Gordon 2001). Care should be taken while interpreting the areal strain rate pattern. For example, the absence of GPS sites along the northeastern boundary of the study area may make the detection of the velocity gradient in east-west direction difficult in the area east and northeast of San Pablo Bay. The relatively good resolution of this part of the solution (figure 5A) can be explained by the unambiguous influence of the damping pushing the model parameters towards zero. The strain rate regime in this area shows almost uniaxial north-south contraction, causing a local minimum in the areal strain rates. However, if the real signal in this region is east-west extension, its detection and modeling would, at least partly, neutralize the negative area change found in our results. Similar data distribution problems may be responsible for (at least part of) the dilatational and contractional signals found at Point Reyes and southeast of Monterey Bay, respectively. It is noteworthy that a 50 km long section of the central Bay / San Pablo Bay shows no resolvable areal strain rate. This was previously noted by Argus and Gordon (2001), who further noted the low topography of this part of the SFBR and explained the relative lack of a contractional signal as due to the local geometry of the faults accommodating the long term strain release. Finally, localization in both shear and areal strain rate may be noted in the epicentral region of the 1989 Loma Prieta earthquake.

3 VISCOELASTIC STRATIFICATION

The basis for forward modeling of SFBR deformation here is the response to imposed dislocation sources of a gravitational viscoelastic coupled medium. The viscoelastic structure used here is shown in figure 7. It consists of an elastic upper crust of thickness 15 km, a Maxwell viscoelastic lower crust of thickness 15 km and viscosity η_c, and a Maxwell viscoelastic upper mantle of viscosity η_m. This structure is one of two alternative structures derived by Pollitz et al. (1998) on the basis of postseismic geodetic observations following the 1989 Loma Prieta earthquake. Their Model B is characterized by a relatively strong crust and weak mantle with $\eta_c/\eta_m = 3.3$ and $\eta_m = 2 \times 10^{19}$ Pa s. We adopt the crust-to-mantle viscosity ratio of that model since it is not well constrained by only horizontal postseismic data, but we allow η_m to vary in order to attain a better estimation of viscosity structure using the present GPS velocity field.

Source parameters must be specified for the two earthquakes most likely associated with significant relaxation effects: the M7.8 1906 and M6.9 1989 Loma Prieta earthquakes. For this purpose we adopt the coseismic fault slip and geometry models of Marshall et al. (1991); Thatcher et al. (1997).

4 EVOLUTION OF DEFORMATION

The regional deformation is envisaged to be composed of three principal physical processes: Horizontal simple shear and fault-perpendicular uniaxial compression driven by Pacific - SNGV relative motion; postseismic relaxation of the viscoelastic Earth following major earthquakes; creep along parts of the San Andreas, Calaveras, and Hayward faults. These elements provide a description of the processes of tectonic loading, time-dependent response due to earthquakes, and fault creep. In spherical r, θ, ϕ coordinates the momentum equation in the Laplace transform domain is (Pollitz 1997)

$$\rho_0 g_0[(\nabla\cdot\mathbf{u}) + \frac{2}{r}(\hat{r}\cdot\mathbf{u})) - \nabla(\hat{r}\cdot\mathbf{u})] + \nabla\cdot\mathbf{T}$$
$$= \left(\sum_j \int d\Sigma_j \mathbf{m}_j(\mathbf{r}', s)\cdot\nabla\delta(\mathbf{r} - r')\right) - \mathbf{f}(\mathbf{r}, s) \quad (4)$$

where ρ_0 and g_0 are density and gravitational acceleration on a spherically symmetric reference model; $\mathbf{m}_j(r', s)$ represents a distribution of dislocation sources (earthquakes or fault creep) on the jth fault surface with area element $d\Sigma_j$; $\mathbf{f}$ represents a distribution of forces associated with tectonic loading; T is the stress tensor:

$$\mathbf{T}_{ij}(\mathbf{r}, s) = \lambda(\mathbf{r}, s)e_{kk}\delta_{ij} + 2\mu(\mathbf{r}, s)e_{ij} \quad (5)$$

$$e_{ij} = \frac{1}{2}(\frac{\partial u_i}{\partial x_j} + \frac{\partial u_j}{\partial x_i}) \quad (6)$$

where $\mathbf{u}(\mathbf{r}, s)$ is the displacement field. Equation 4 accounts for the first-order coupling of viscoelastic deformation with Earth's gravitational acceleration; the second order effect of coupling with changes in gravitational potential is neglected. This approximation is sometimes referred to in the seismological literature as Cowling's approximation (Dahlen and Tromp 1998). We assume relaxation of a Maxwell viscoelastic solid:

$$\kappa(\mathbf{r}, s) = \kappa_0,$$
$$\mu(\mathbf{r}, s) = \frac{\mu_0 s}{s + \frac{\mu_0}{\eta}} \quad (7)$$

where κ_0, μ_0 are the static elastic constants and η is the viscosity. All quantities dependent on s are evaluated in the Laplace transform domain. Equations 4-7 are to be solved subject to boundary conditions $\hat{r}\cdot T = 0$ at Earth's surface (vanishing traction at Earth's surface) and an appropriate interior boundary condition (for example, vanishing displacement at an arbitrarily specified interior interface).

In principle, equations 4-7 should be solved with a three-dimensional distribution of isotropic elastic parameters κ and μ. However, the main variations of κ and μ are with depth, and we assume that the remaining lateral variations are controlled by the presence of thick lithospheric blocks bounding the plate boundary zone, i.e., the Pacific plate and SNGV lithosphere. (This produces a large contrast in $\mathbf{u}(\mathbf{r}, s)$ at all depths, including those beneath the elastic plate thickness assigned to the plate boundary zone.) This situation is well approximated by a kinematic boundary condition of constant Pacific - SNGV relative velocity applied on the edges of the shear zone (figure 2). Our strategy is then to write the solution for $\mathbf{u}$ and $\mathbf{T}$ on the 3D model in terms of the solution on the equivalent 1D model with depth-dependent material properties corresponding to those of the shear zone:

$$\rho_0 g_0[(\nabla\cdot\mathbf{u}) + \frac{2}{r}(\hat{r}\cdot\mathbf{u})) - \nabla(\hat{r}\cdot\mathbf{u})] + \nabla\cdot\mathbf{T}$$
$$= \left(\sum_j \int d\Sigma_j \mathbf{m}_j(\mathbf{r}', s)\cdot\nabla\delta(\mathbf{r}-r')\right) - [\mathbf{f}(\mathbf{r}, s) + \mathbf{f}_{eq}(\mathbf{r}, s)] \quad (8)$$

where f_{eq} represents a distribution of equivalent forces (which would be applied in the volume outside of the plate boundary zone) needed to satisfy the kinematic boundary conditions. For points $\mathbf{r}$ located on or within the plate boundary zone, the solution of $\mathbf{u}$ and $\mathbf{T}$ in equation 4 on the 3D model is very nearly the same as the corresponding solution of equation 8 on the 1D model.

It is not necessary to know $\mathbf{f}$ or $\mathbf{f}_{eq}$ explicitly; for brevity we refer to the sum $\mathbf{f} + \mathbf{f}_{eq}$ as simply $\mathbf{f}$. We construct a set of special solutions on the equivalent 1D model involving specific dislocation sources $\mathbf{m}_j$ and physically plausible forces $\mathbf{f}$. These special solutions and the associated velocity fields $v = \partial u/\partial t$ are described in the time domain as follows:
(A) Velocity field $\mathbf{v}_{ps}(\mathbf{r}, t)$. Viscoelastic relaxation following specified earthquakes, $\mathbf{m}_j \neq 0$, $\mathbf{f} = 0$ globally.
(B) Velocity field $\mathbf{v}_{shear}(\mathbf{r}, t)$. Horizontal simple shear along vertical planes locally tangent to the curvilinear plate boundary (figure 1), $\mathbf{m}_j = 0$, $\mathbf{f} = 0$ within the plate boundary zone, $\mathbf{f} \neq 0$ outside the plate boundary zone.
(C) Velocity field $\mathbf{v}_{rot}(\mathbf{r}, t)$. Rigid rotation, $\mathbf{m}_j = 0$, $\mathbf{f} = 0$ globally.
(D) Velocity field $\mathbf{v}_{compr}(\mathbf{r})$. Uniaxial horizontal contraction directed perpendicular to vertical planes locally tangent to the curvilinear plate boundary, $\mathbf{m}_j = 0$, $\mathbf{f} = 0$ within the plate boundary zone, $\mathbf{f} \neq 0$ outside the plate boundary zone.
Note that while both $\mathbf{v}_{shear}(\mathbf{r}, t)$ and $\mathbf{v}_{rot}(\mathbf{r}, t)$ may have arbitrary time dependence, $\mathbf{v}_{compr}(\mathbf{r})$ is assumed to be independent of time. Specifically, in a local (East, North) Cartesian coordinate system these velocity fields take the form

$$\mathbf{v}_{shear} = v_1(t)(\frac{\delta}{W}) \times (-\sin\phi, \cos\phi) \quad (9)$$

$$\mathbf{v}_{compr} = v_2(\frac{\delta}{W}) \times (\cos\phi, \sin\phi) \quad (10)$$

where δ is the distance measured positive of a point on or within the plate boundary from the SNGV plate boundary; $W = 135$ km is the width of the plate boundary; ϕ is the strike of the vertical plane locally parallel to the plate boundary. This strike depends upon the geometry of the plate boundary zone (yellow lines in figure 2). The boundaries are meant to approximate the physical boundaries of the plate boundary zone, i.e., the eastern edge of the Coast Ranges on the SNGV side and the offshore faults on the Pacific side. The given boundaries were determined by a process of trial and error. They are specified as small circles about a pole $\hat{\Omega}_1$ located at angular distances 17.82° and 19.04° from the pole (figure 8). The local azimuth of a small circle about this pole through a given point defines ϕ. We can then write

$$\mathbf{v}_{shear} = -\left(\frac{v_1(t)}{sin(19.04^\circ)}\right)(\frac{\delta}{W})\hat{\Omega}_1\times\hat{r} \quad (11)$$

for points $\hat{r}$ located in the plate boundary zone. Similarly we define a pole $\hat{\Omega}_2$ to be 90° from the plate boundary zone along an azimuth tangent to it (figure 8). We then have

$$\mathbf{v}_{compr} = -v_2(\frac{\delta}{W})\hat{\Omega}_2\times\hat{r} \quad (12)$$

Note that the solution for $\mathbf{v}_{shear}$ in equation 11 is a valid solution of equation 8 even for time-dependent $v_1(t)$, whereas the corresponding solution for $\mathbf{v}_{compr}$ in equation 12 is valid only for constant v_2. Time-dependent v_2 would produce transient shear strains which relax with time and would modify the solution in equation 12. In order to account for the additional relaxation would require explicit dependence upon the history of v_2. In the subsequent process of matching boundary conditions, it is convenient to have a direct relationship between $\mathbf{v}_{shear}$ or $\mathbf{v}_{comp}$ on the plate boundaries and the corresponding velocity fields within the plate boundary. The choice of time-independent v_2 is thus somewhat limiting but allows this approach to be carried out straightforwardly and greatly simplifies the analysis.

A fifth component of the model velocity field is that associated with creep on SFBR faults: $\mathbf{v}_{creep}(\mathbf{r})$. The principal creeping fault segments are shown in figures 2 and 11E. We prescribe a-priori the behavior on these creeping faults by specifying the depth range and rate of slip as follows. Hayward fault, 0-5 km, 5 mm/yr based on Simpson et al. (2001); Central SAF, 0-15 km, variable slip rate 12-30 km/yr (Rymer et al. 1984); NW creeping segment, 0-15 km, 12 mm/yr; S. Calaveras fault, 0-15 km, 12 mm/yr (Oppenheimer et al. 1990). The velocity field produced by steady creep prescribed by these dislocations is evaluated in the fluid limit of the viscoelastic model in a spherical geometry using the method of Pollitz (1996).

The model velocity field at point $\mathbf{r}$ in a fixed SNGV reference frame may be written in the time domain as follows:

$$\mathbf{v}(\mathbf{r}, t|SNGV) = \mathbf{v}_{shear}(\mathbf{r}, t) + \mathbf{v}_{compr}(\mathbf{r}) + \mathbf{v}_{ps}(\mathbf{r}, t)$$
$$+\Omega\times\mathbf{r} + \mathbf{v}_{creep}(\mathbf{r}) \quad (13)$$

In order to compare the model velocity field with the GPS velocity field it is necessary to apply an addition SNGV - North America (NA) rotation:

$$\mathbf{v}(\mathbf{r}, t|NA) = \mathbf{v}(\mathbf{r}, t|SNGV) + \Omega_{SNGV-NA}\times\mathbf{r} \quad (14)$$

5 MODEL OF SFBR DEFORMATION

5.1 Estimation of model parameters

The model velocity field with respect to fixed SNGV in equation 13 depends upon v_1, v_2, η_m, and Ω (three components). The model velocity field with respect to fixed NA further depends upon

$\Omega_{SNGV-NA}$. We require that $\mathbf{v}(\mathbf{r}, t|SNGV)$ be consistent with constant Pacific - SNGV boundary conditions. To make this more precise it is convenient to define the SNGV-Pacific angular velocity vector as the composite of fault-parallel and fault-perpendicular motions:

$$\mathbf{\Omega}_{SNGV-Pac} = \frac{v_{pl}}{sin(19.04^\circ)}\hat{\Omega}_1 + v_2\hat{\Omega}_2 \tag{15}$$

where v_{pl} is the magnitude of Pacific - SNGV relative motion parallel to the plate boundary. We require that

$$\mathbf{v}(\mathbf{r}_i, t|SNGV) = -\mathbf{\Omega}_{SNGV-Pac}\times\mathbf{r}_i \tag{16}$$

for points $\mathbf{r}_i$ located on the Pacific plate boundary, and

$$\mathbf{v}(\mathbf{r}_i, t|SNGV) = \mathbf{0} \tag{17}$$

for points $\mathbf{r}_i$ located on the SNGV plate boundary.

The strategy for determining the various parameters is:

(i) Estimate v_1 and rotation Ω for a given η_m by least squares inversion such that $\mathbf{v}(\mathbf{r}_i, t|SNGV)$ satisfies the above boundary conditions with optimally small error. Note that v_2 is indeterminate in this step because of its common appearance in equations 13 and 16.

(ii) Determine additionally v_2 and the rotation $\Omega_{SNGV-NA}$ which minimizes the reduced χ^2

$$\chi^2 = \frac{1}{N-M}(\mathbf{v}_{model} - \mathbf{v}_{obs})^T \cdot \mathbf{C}^{-1} \cdot (\mathbf{v}_{model} - \mathbf{v}_{obs}) \tag{18}$$

where $\mathbf{v}$ is a composite velocity vector consisting of all model or observed velocity components at the $N = 102$ employed GPS sites, and $\mathbf{C}$ is the data covariance matrix. $M = 6$ is the number of independent parameters.

(iii) Repeat the above two steps with a grid search over η_m in order to find the optimum simultaneous fit of both the boundary conditions and the GPS data.

For purposes of illustrating sensitivity to the model parameters, one may remove one of the parameters (say, v_2) from the inversion process in step (i) and include it together with η_m as a grid search parameter in step (iii).

5.2 Results

The above procedure has been carried out using a range of possible relative plate velocities v_{pl}. Results are very similar for 37 mm/yr $< v_{pl} <$ 40 mm/yr. We choose the value $v_{pl} = 38$ mm/yr for further consideration.

The best-fitting model is specified by $\eta_m = 1.2 \times 10^{19}$ Pa s, $v_1 = 32$ mm/yr, $v_2 = 3$ mm/yr, $\Omega = (39.326^\circ$ N -118.509°E $0.594^\circ/Myr)$ (clockwise rotation), and $\Omega_{SNGV-NA} = (48.575^\circ$ N -115.128°E $0.490^\circ/Myr)$ (figure 9, clockwise rotation). From equation 15 this yields $\mathbf{\Omega}_{SNGV-Pac} = (44.64^\circ$N -99.34°E $1.081^\circ/Myr)$ (figure 8). The sensitivity of model fit to η_m and v_2 is shown in figure 10, which indicates a strong minimum in these parameters.

Inference of these parameters is dependent upon the choice of plate boundaries. The Pacific and SNGV plate boundaries in figure 2 are small circles about $\hat{\Omega}_1$ in figure 8. Because the $\mathbf{v}_{shear}$ component rotates if $\hat{\Omega}_1$ is changed, a change in $\hat{\Omega}_1$ will introduce a tradeoff between inferred $\mathbf{v}_{shear}$ and $\mathbf{v}_{compr}$. Consequently, the value of best-fitting v_2 is very sensitive to the choice of $\hat{\Omega}_1$. However, the inferred SNGV-Pacific angular velocity vector $\mathbf{\Omega}_{SNGV-Pac}$ and, consequently, predicted model deformation are practically insensitive to this choice. For example, if $\hat{\Omega}_1$ were chosen 1° farther north, inferred v_2 would increase to 4 mm/yr, but the compounded effect of these changes on $\mathbf{\Omega}_{SNGV-Pac}$ when propagated through equation 15 is negligible. Therefore the pole location of $\mathbf{\Omega}_{SNGV-Pac}$ shown in figure 8 is largely insensitive to initial assumptions. It is located just south of the 95% confidence region for this motion obtained by Argus and Gordon (2001). Argus and Gordon (2001) derived plate motions using very different geodetic data which includes sites on the southern SNGV plate. Considering that the present data set is confined to the northern boundary of the SNGV plate, we suggest that either the formal errors in the Argus and Gordon (2001) determination of SNGV-Pacific motion are too small, or there are subtle differences between SNGV motion in the SFBR and its motion further south. The second possibility is also suggested by the fact that our $\mathbf{\Omega}_{SNGV-Pac}$ pole and that of Murray and Segall (2001) both lie to the northeast of the plate boundary zone (clockwise motion) whereas other estimates of $\mathbf{\Omega}_{SNGV-Pac}$ lie to the southwest of the plate boundary zone (counterclockwise motion) (figure 9). Ours and Murray and Segall's estimate are based on data from the SFBR whereas the other estimates are based on data more broadly distributed over the SNGV plate.

The five components of the model velocity field are shown in figure 11. It is clear that most (about 85%) of the simple shear being accommodated in the plate boundary zone is represented by $\mathbf{v}_{shear}$. The remaining 15% is accommodated by $\mathbf{v}_{ps}$ primarily through viscoelastic relaxation following the 1906 earthquake. The total model velocity field with respect to fixed SNGV obtained by summing these five components is shown in figure 12. There is excellent agreement between the model velocity field and the imposed relative velocity boundary condition given by equation 16, which is a combination of 38 mm/yr fault-parallel and 3 mm/yr fault-perpendicular motion.

6 DISCUSSION

The total model velocity field with respect to fixed North America is shown in figure 13, where it may be compared with the GPS velocity field. The two velocity fields are in very good agreement, and it is difficult to identify systematic biases, even near creeping faults, suggesting that the creep model described in section 4 accounts for the main discontinuities observed in the regional velocity field. We compute the piece-wise continuous velocity gradient field for the modeled velocity field by application of the same method under the same conditions for parameterization and regularization as described in section 2.2. We use a uniform value for the a priori data standard deviation of 1.2 mm/yr, which is the average standard deviation of the GPS velocity data. The inversion characteristics of the final gradient field of the modeled velocity field are very similar to those of the GPS derived solution: $size[\boldsymbol{S}] = 1233$, $size[\boldsymbol{C}] = 3.3 \cdot 10^{-5}/yr$, root mean square misfits of 1.0 for the GPS data and 1.5 for the extra data constraints. The velocity gradient fields associated with the modeled and observed velocity fields (figure 6) agree very well. The greater concentration of pure shear and rotation rates (approximately equal to simple shear strain rate) around the San Andreas fault is exhibited in both strain rate fields. The pattern of areal strain rates are also similar. The small differences which exist are mainly in amplitude rather than pattern. Thus the large contractile strain rates observed in the NE part of transect 1 and near the Loma Prieta rupture zone, as well as the dilatational strain rates observed near Point Reyes, are also present in the

modeled strain pattern but with reduced amplitude. Overall, the observed dilatational strain rates (figure 6B) are uniform over most of the SFBR where resolution is relatively good (figure 5A). A similar uniformity in modeled strain rate pattern characterizes our solution (figure 6E). Except for the northeastern part of transect 1, where modeled dilatation rate does not match the observed contraction and where no local post-earthquake effects have been accounted for, the assumption of uniform regional contraction (equation 12) appears to be a good approximation. If regional contraction is indeed manifested over several earthquake cycles within a localized band, this feature is not exhibited during the present interseismic period.

The curvilinear boundaries shown in Figure 2 are intended to represent the average trend of the Pacific-SNGV plate boundary at any given location. The trend defined by those curves varies from N31.7°W in the north (Lake Berryessa) to N36.8°W in the south (Calaveras-SAF junction). The plate boundary so defined closely follows the average trend of the major faults at any given latitude. For example, Argus and Gordon (2001) found an average strike-slip fault trend of N33.9°W across Lake Berryessa (profile I-I' in their Figure 3), N33.1°W across the San Francisco Peninsula (profile G-G'), and N37.5°W near the Calaveras-SAF junction (profile E-E'). Comparison of such average fault trends with the local relative Pacific-SNGV motion vector determined by those authors leads to fault-perpendicular convergence rates varying from 1.8 to 3.3 mm/yr (except in the San Pablo Bay zone, which is undergoing a small amount of fault-perpendicular extension), close to the value of 2.9 mm/yr determined in our study. In an independent study, Savage et al. (2003) have determined an average regional fault-perpendicular contraction rate of 0.9 ± 1.1 mm/yr, i.e. a regional extension that is statistically indistinguishable from zero. This estimate is based on the fact that the best-fitting uniform horizontal strain field for the region is characterized by principal strain rates of $\epsilon_{11} = 164.7 \pm 7.2$ nanostrain/yr and $\epsilon_{22} = -157.9 \pm 6.9$ oriented N74.0°W and N16.0°E, respectively. This is equivalent to a combination of pure shear of 161.4 ± 5.0 nanostrain/yr oriented N28.4°W and 6.9 ± 7.9 nanostrain/yr of uniaxial extension perpendicular to this direction. Savage et al. (2003) suggests that 0.9 ± 1.1 mm/yr should be representative of the regional fault-perpendicular compression, which would imply regional extension at a statistically insignificant level. However, we note that the average fault trend is $\sim$ N33.5°W, documented by Argus and Gordon (2001). Use of that trend in the presence of the derived uniform strain rate field would result in ~ 3 mm/yr fault-perpendicular compression, similar to the other estimates.

The agreement between observed and modeled strain rate fields is attributed in part to the effect of postseismic relaxation. The strain rate field associated with post-1906 and post-1989 relaxation is shown in figure 14. It suggests that the greater concentration of shear strain rate near the San Andreas fault is due in large part to post-1906 relaxation which persists more than 90 years after the earthquake. Such behavior is also predicted in fully numerical finite element models that include viscoelastic elements within parts of the lower crust and mantle (e.g., Figure 2b of Kenner and Segall 1999). Similarly, part of the observed shear and areal strain rate maxima near the Loma Prieta rupture zone are attributed to post-1989 relaxation.

7 CONCLUSIONS

Strain accumulation in the SFBR can be described to first order as the product of simple shear within a ~ 135 km wide plate boundary zone combined with minor fault-perpendicular compression, lingering effects of postseismic relaxation following the 1906 San Francisco and 1989 Loma Prieta earthquakes, and the effects of steady fault creep. This physical model has been calibrated to optimally fit a set of 102 GPS velocity vectors by a grid search for both the degree of fault-perpendicular compression and the viscoelastic parameters that govern the behavior of the plate boundary zone. With a mantle viscosity of 1.2×10^{19} Pa s and a regional fault-perpendicular compression of ~ 3 mm/yr, there is excellent agreement between the observed and modeled velocity field. Slightly greater strain rates centered around the San Andreas fault proper (about 20 nanostrain greater than the average 140 nanostrain for the entire plate boundary) at present is attributed to postseismic relaxation following the 1906 earthquake. The driving forces in this model are horizontal forces transmitted by the relatively thick Pacific and SNGV blocks to the plate boundary zone along its edges. This physical model is not unique but, if applicable, it suggests that previously considered loading mechanisms involving continual slip beneath a "locking depth" are not necessary in order to explain the main features of the strain accumulation pattern.

ACKNOWLEDGMENTS

We are grateful to Weijun Gan and Will Prescott for making available to us the processed GPS data set used in this study. We thank Jim Savage and other members of the Crustal Strain Group at USGS for discussions.

REFERENCES

Argus, D.F. & Gordon, R.G., 2001. Present tectonic motion across the Coast Ranges and San Andreas fault system in central California, *Geol. Soc. Am. Bull.*, **113**, 1580-1592.

Bakun, W.H., 1999. Seismic activity of the San Francisco Bay region, *Bull. seismol. Soc. Am.*, **89**, 764-784.

Dahlen, F. A., & Tromp, J., 1998. *Theoretical Global Seismology*, (Princeton University Press, Princeton).

Dixon, T.H., Miller, M., Farina, F., Wang, H.Z., & Johnson, D., 2000. Present-day motion of the Pacific-North America plate boundary zone, *Tectonics*, **19**, 1-24.

Eberhart-Phillips, D., & Reyners, M., 1997. Continental subduction and three-dimensional crustal structure: The northern South Island, New Zealand, *J. geophys. Res.* , **102**, 11,843-11,861.

Kenner, S.J., & Segall, P., 1999. Time dependence of the stress shadowing effect and its relation to the structure of the lower crust, *Geology*, **27**, 119-122.

Marshall, G.A., Stein, R.S., & Thatcher, W., 1991. Faulting geometry and slip from co-seismic elevation changes: The October 17, 1989 Loma Prieta earthquake, *Bull. seismol. Soc. Am.*, **81**, 1660-1693.

Menke, W., 1989. Geophysical Data Analysis: Discrete Inverse Theory, *International Geophysics Series*, **45**, (revised ed., 289 pp., Academic Press, San Diego).

Michelini, A., & McEvilly, T. V., 1991. Seismological studies of Parkfield, 1. Simultaneous inversion for velocity structure and hypocenters using cubic b-splines parameterization, *Bull. seismol. Soc. Am.* , **81**, 524-552.

Murray, M.H. & Segall, P., 2001. Modeling broadscale deformation in northern California and Nevada from plate motions and elastic strain accumulation, *Geophys. Res. Lett.*, **28**, 4315-4318.

Oppenheimer, D.H., Bakun, W.H., & Lindh, A.G., 1990. Slip partitioning of the Calaveras fault, California, and prospects for future earthquakes, *J. geophys. Res.*, **95**, 8483-8498.

Parsons, T., 2002. Post-1906 stress recovery of the San Andreas fault system calculated from three-dimensional finite element analysis, *J. geophys. Res.*, **107**, ESE 3 1-13.

Pollitz, F.F., 1996. Coseismic deformation from earthquake faulting on a layered spherical Earth, *Geophys. J. Int.*, **125**, 1-14.

Pollitz, F.F., 1997. Gravitational-viscoelastic postseismic relaxation on a layered spherical Earth, *J. geophys. Res.*, **102**, 17921-17941.

Pollitz, F.F., Bürgmann, R., & Segall, P., 1998. Joint estimation of afterslip rate and postseismic relaxation following the 1989 Loma Prieta earthquake, *J. geophys. Res.*, **103**, 26975-26992.

Prescott, W.H., Savage, J.C., Svarc, J.L., & Manaker, D., 2001. Deformation across the Pacific-North America plate boundary near San Francisco, California, *J. geophys. Res.*, **106**, 6673-6682.

Rymer, M.J., Lisowski, M., & Burford, R.O., 1984. Structural explanation for low creep rates on the San Andreas fault near Monarch Peak, central California, *Bull. seismol. Soc. Am.*, **74**, 925-931.

Savage, J.C., Simpson, R.W., & Murray, M.H., 1998. Strain accumulation rates in the San Francisco Bay area, 1972-1998, *J. geophys. Res.*, **103**, 18,039-18,051.

Savage, J.C., Gan, W., Prescott, W.H., & Svarc, J.L., 2003. Strain accumulation across the Coast Ranges at the latitude of San Francisco, *submitted*.

Segall, P., Bürgmann, R., & Matthews, M., 2000. Time dependent deformation following the 1989 Loma Prieta earthquake, *J. geophys. Res.*, **105**, 5615-5634.

Simpson, R.W., Lienkaemper, J.J., & Galehouse, J.S., 2001. Variations in creep rate along the Hayward fault, California interpreted as changes in depth of creep, *Geophys. Res. Lett.*, **28**, 2269-2272.

Spakman, W., & Nyst, M. C. J., 2002. Inversion of relative motion data for estimates of the velocity gradient field and fault slip, *Earth planet. Sci. Lett.*, **203**, 577-591.

Thatcher, W., 1983. Nonlinear strain builup and the earthquake cycle on the San Andreas fault, *J. geophys. Res.*, **88**, 5893-5902.

Thatcher, W., Marshall, G., & M. Lisowski, 1997. Resolution of fault slip along the 470-km-long rupture of the great 1906 San Francisco earthquake and its implications, *J. geophys. Res.*, **102**, 5353-5367.

Working Group on California Earthquake Probabilities, 1999. Earthquake probabilities in the San Francisco Bay Region: 2000 to 2030, A summary of findings, *Open File Rep.*, **99-517**, U.S. Geol. Surv., Reston, VA.

This paper has been produced using the Blackwell Scientific Publications GJI LaTeX2e class file.

Figure 1. Map of San Francisco Bay Region indicating major faults.

Figure 2. GPS velocity field from 1994 to 2000 with 95% confidence regions (Savage et al. 1998). Boundaries between the 135 km-thick plate boundary zone and the Pacific and SNGV plates indicated by yellow lines, each of which is a small circle about a common Euler pole.

Figure 3. (A) Each of the six SW-NE profiles that compose the GPS velocity field are depicted with black line segments and labeled with boxed numerals. (B) Representation of the velocity field in terms of fault-parallel and fault-perpendicular components. These directions are specified by N33.85°W and N56.15°E, respectively for profiles 1 - 3 and N40°W and N50°E, respectively for profiles 4 - 6. SAF: San Andreas fault. RC: Rodgers Creek and Hayward faults. GV: Concord-Green Valley and Calaveras faults. X=0 corresponds with the intersection of the particular transect with the San Andreas fault.

Figure 4. Sensitivity analysis of inversions of GPS velocity data (figure 2) for the velocity gradient field. Results for $size[\boldsymbol{C}]$ (equation 2, figures A), $size[\boldsymbol{S}]$ (equation 3, figures B), the root-mean-square misfit of the $\boldsymbol{\nabla} \times \boldsymbol{\nabla v} = \mathbf{0}$ constraints (figures C) and the GPS data equations (figures D) for varying weights on damping (α_d, along y-axes), smoothing (α_s, along x-axes) and $\boldsymbol{\nabla} \times \boldsymbol{\nabla v} = \mathbf{0}$ constraints (γ_r, subplots 1, 2 and 3). Every contour plot represents 25 inversions.

Figure 5. Quality in terms of resolution and model variance of the velocity gradient field computed from the GPS velocity data (figure 2): Diagonal resolution of the model parameters: partial derivatives of the velocity field in (A) longitudinal and (B) latitudinal direction. Contours are plotted at 10% intervals (every 0.1); (C) The resolution spread function with contours at intervals of 2; (D) Model standard deviations (i.e., 1-σ errors) with contours at intervals of $1{\cdot}10^{-8}$/yr. The model error pattern for derivatives in longitudinal direction is almost similar to the pattern for derivatives in latitudinal direction.

Figure 6. Components of the velocity gradient field derived from the GPS velocity field (A, B and C) and the best-fitting model velocity field (D, E and F). Plots A and D represent the second invariant of the strain rate tensor (i.e., pure shear) and indicate the axes of maximum rates of contraction and extension with black and white line segments, respectively, with magnitudes proportional to the lengths of these segments. Plots B and E represent the first invariant of the strain rate tensor (i.e., areal strain rate) with C and E indicative for rates of contraction and extension, respectively, plots C and F represent the rotation rate tensor (i.e., the anti-symmetric part of the velocity gradient tensor) with CW and CCW indicative for clockwise and counterclockwise. Superimposed dots indicate GPS sites. Contours are plotted at intervals of $1{\cdot}10^{-7}$/yr, with blue for positive, red for negative and green for zero values.

Figure 7. One-dimensional viscoelastic stratification of the SFBR assumed in this study, following Model B of Pollitz et al. (1998).

Figure 8. The SNGV-Pacific relative plate motion is decomposed into a "fault-parallel" component parallel to small circles about $\hat{\Omega}_1$ ($48.0°$N, $-100.0°$E) and a "fault-perpendicular" component parallel to small circles about $\hat{\Omega}_2$ ($-41.1°$N, $-74.1°$E). The SNGV-Pacific plate boundary zone is delineated by two small circles about $\hat{\Omega}_1$ at angular distances of $17.82°$ and $19.04°$. After estimation of the regional fault-perpendicular velocity v_2, the SNGV-Pacific angular velocity vector $\mathbf{\Omega}_{SNGV-Pac}$ is obtained from equation 15 : ($44.64°$N $-99.34°$E $1.081°/Myr$) (triangle). Plotted ellipse indicates the SNGV-Pacific angular velocity vector and 95% confidence ellipse obtained by Argus and Gordon (2001). The upper plot shows a closer view of the boxed region in the lower plot.

Figure 9. Estimated SNGV-North America angular velocity vector and 95% confidence region obtained in this study. Alternative estimates are by Murray and Segall (2001) (circle), Argus and Gordon (2001) (star), and Dixon et al. (2000) (square).

Figure 10. Results of grid search for η_m and v_2 to minimize reduced χ^2 (equation 18). The best-fitting model is obtained at $\eta_m = 1.2 \times 10^{19}$ Pa s and $v_2 = 2.9$ mm/yr.

Figure 11. Components of the average 1994 - 2000 velocity field calculated from the best-fitting model. (A) field $\mathbf{v}_{ps}$, (B) $\mathbf{v}_{shear}$, (C) field $\mathbf{v}_{rot}$, (D) $\mathbf{v}_{compr}$, (E) $\mathbf{v}_{creep}$. Each velocity field is calculated at the 102 GPS sites as well as 20 points on the plate boundary. Each of the Pacific and SNGV plate boundaries are sampled at 10 uniformly spaced locations.

Figure 12. The total model velocity field $\mathbf{v}(\mathbf{r}, 1994 - 2000|SNGV)$ (equation 13) evaluated at the 102 GPS sites and 20 plate boundary sites are shown by the black vectors. The imposed relative Pacific - SNGV velocity boundary condition prescribed by equations 16 and 17 are shown by the red vectors. In equation 13 we take $v_{pl} = 38$ mm/yr and $\mathbf{v}_{compr}$ given by equation 10 with $v_2 = 2.9$ mm/yr. (The boundary condition and model velocity vectors are plotted at 10 sample points on both the Pacific and SNGV boundaries. They are negligible on the SNGV boundary.)

Figure 13. Total model velocity field $\mathbf{v}(\mathbf{r}, 1994 - 2000|NA)$ (black arrows) calculated from equation 14, and GPS velocity field (red arrows).

Figure 14. Strain rate pattern due to viscoelastic relaxation following the 1906 and 1989 earthquakes, derived from the corresponding velocity field of figure 11E. (A) Pure shear strain rates; (B) Areal strain rates; (C) Rotation rates. Contours are plotted at $5{\cdot}10^{-8}$/yr intervals, with blue for positive, red for negative and green for zero values.

Figure 1

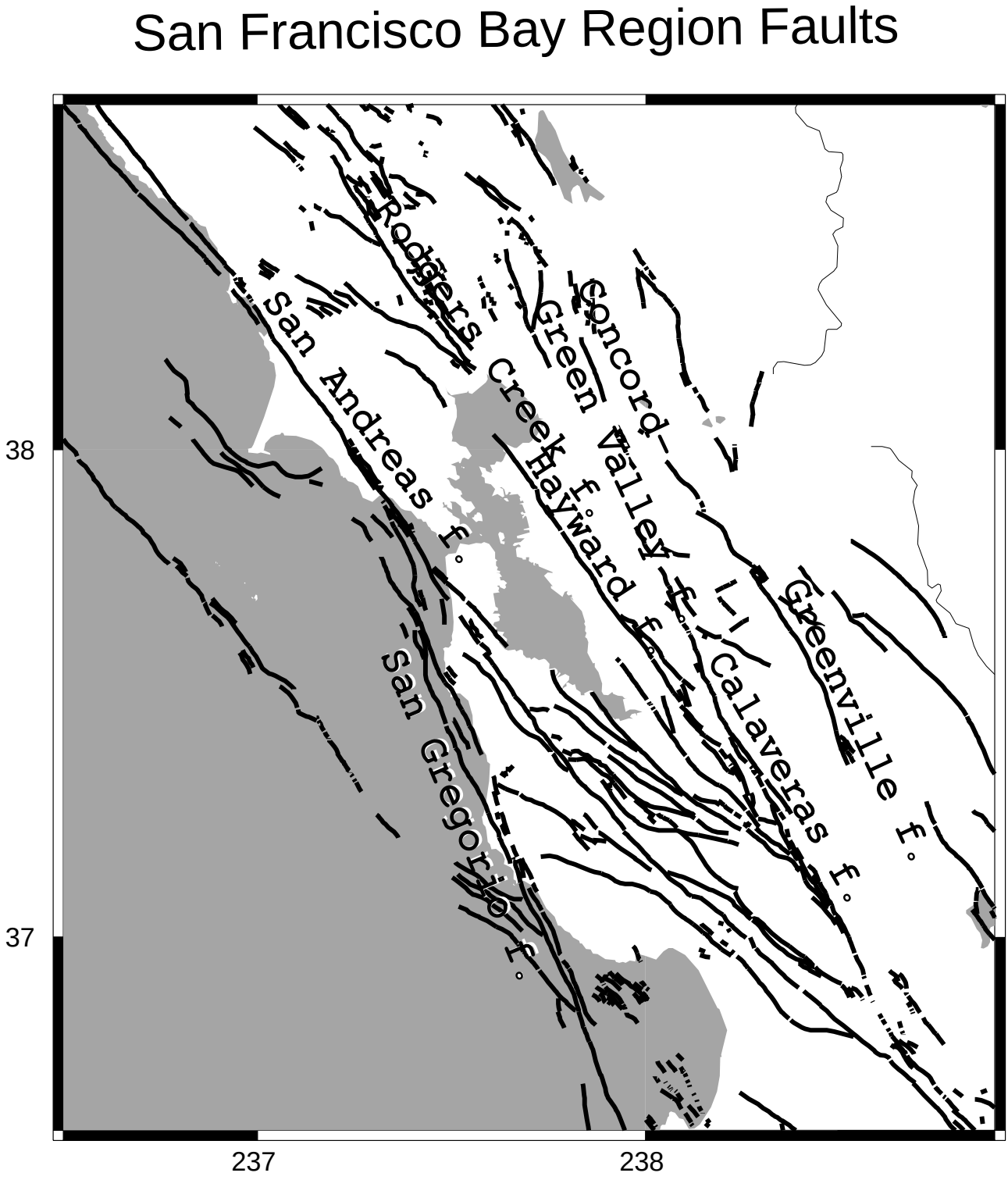
San Francisco Bay Region Faults
Rodgers
Green Valley f.
Concord-
Calaveras f.
Greenville f.
San Andreas f.
Hayward f.
Creek
San Gregorio f.
38
37
237
238

Figure 2

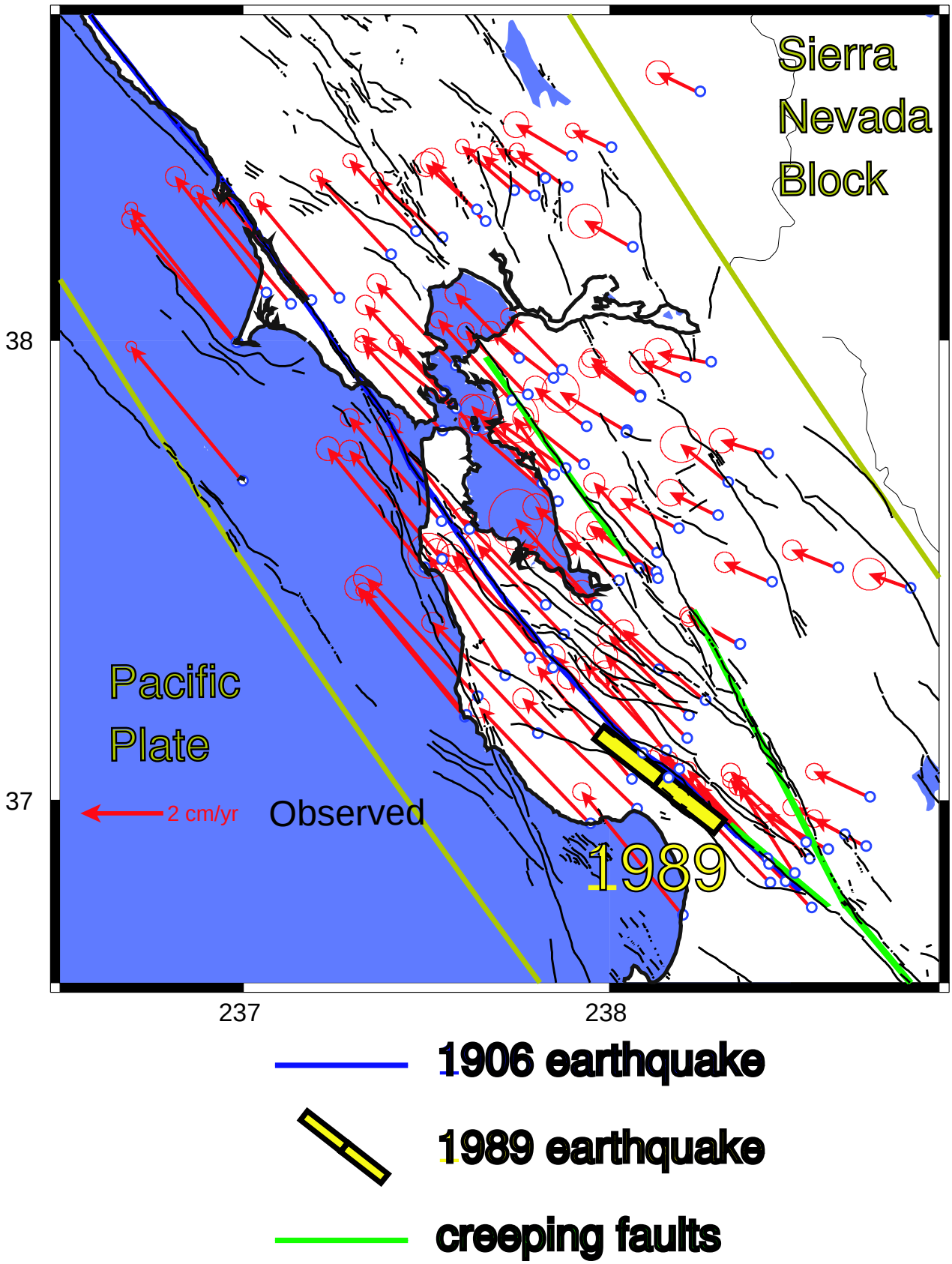
Sierra
Nevada
Block
Pacific
Plate
2 cm/yr
Observed
1989
38
37
237
238
1906 earthquake
1989 earthquake
creeping faults

Figure 3

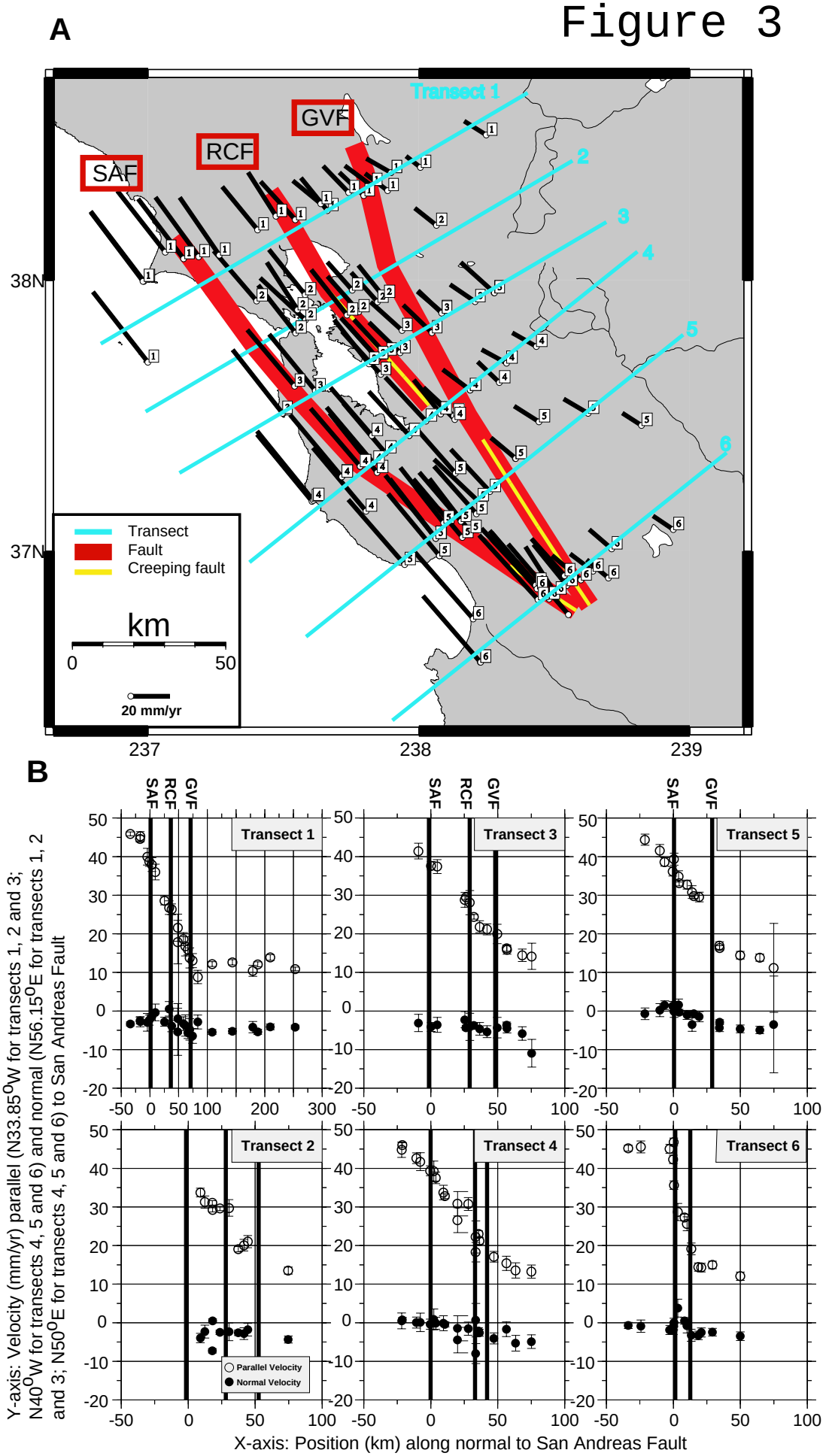
A
Transect 1
2
3
4
5
6
GVF
RCF
SAF
38N
37N
Transect
Fault
Creeping fault
km
0
50
20 mm/yr
237
238
239
B
SAF
RCF
GVF
Transect 1
Transect 3
Transect 5
Transect 2
Transect 4
Transect 6
Parallel Velocity
Normal Velocity
Y-axis: Velocity (mm/yr) parallel (N33.85°W for transects 1, 2 and 3; N40°W for transects 4, 5 and 6) and normal (N56.15°E for transects 1, 2 and 3; N50°E for transects 4, 5 and 6) to San Andreas Fault
X-axis: Position (km) along normal to San Andreas Fault

Figure 4

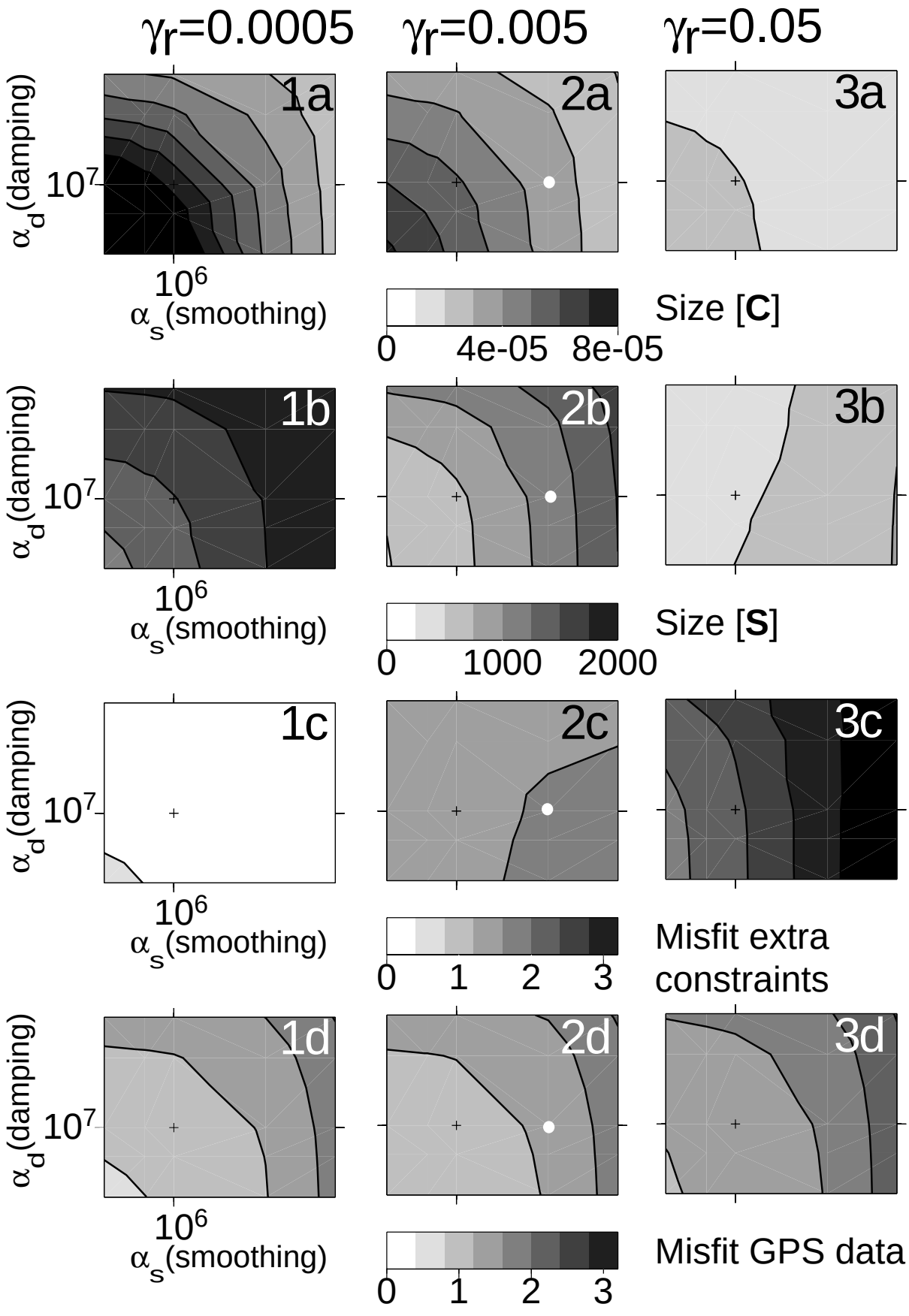
γr=0.0005
γr=0.005
γr=0.05
1a
2a
3a
1b
2b
3b
1c
2c
3c
1d
2d
3d
αd(damping)
10^7
10^6
αs(smoothing)
Size [C]
0
4e-05
8e-05
Size [S]
1000
2000
Misfit extra constraints
Misfit GPS data
1
2
3

Figure 5

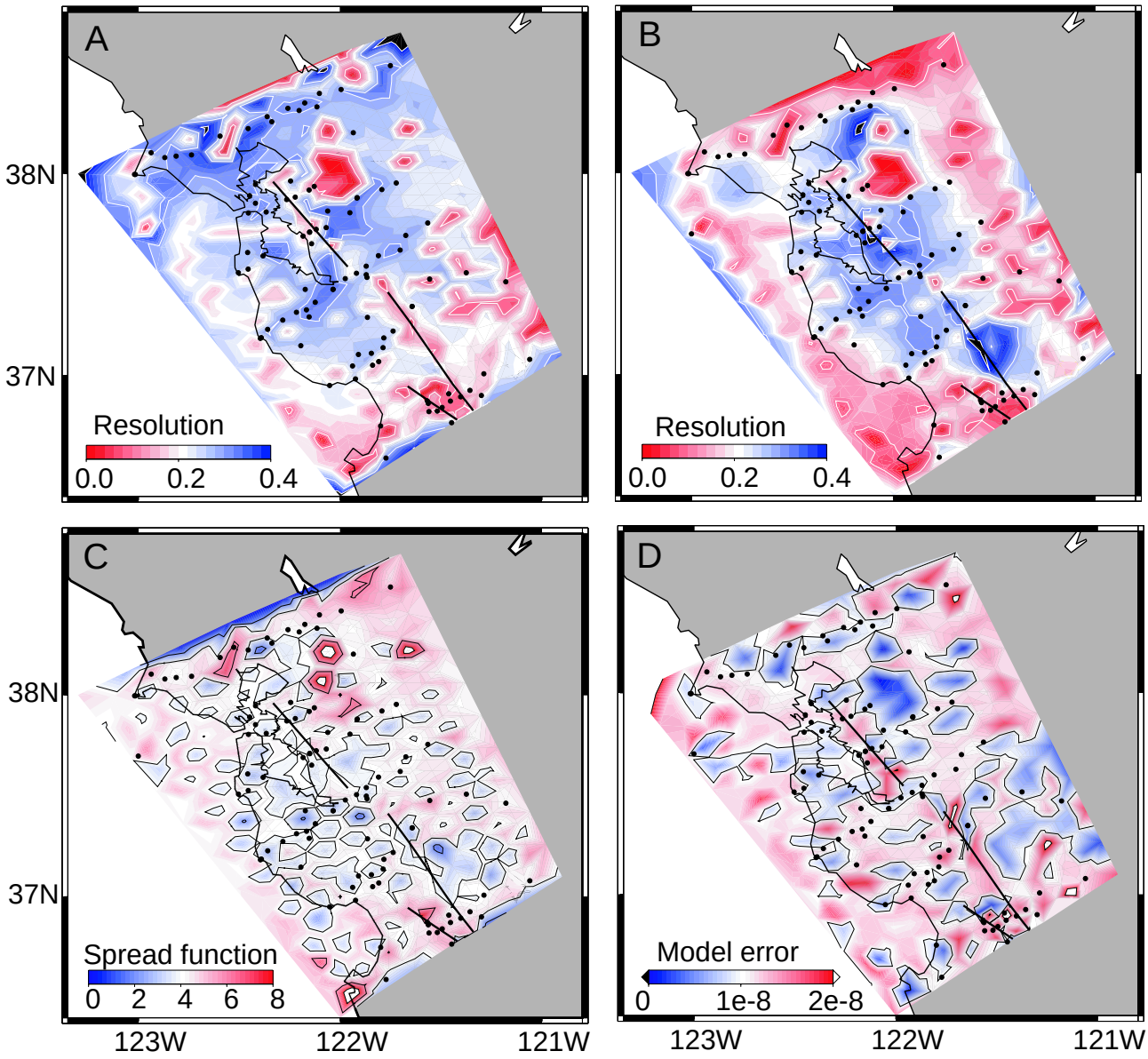
A
B
C
D
38N
37N
Resolution
0.0
0.2
0.4
Spread function
0
2
4
6
8
Model error
0
1e-8
2e-8
123W
122W
121W

Figure 6

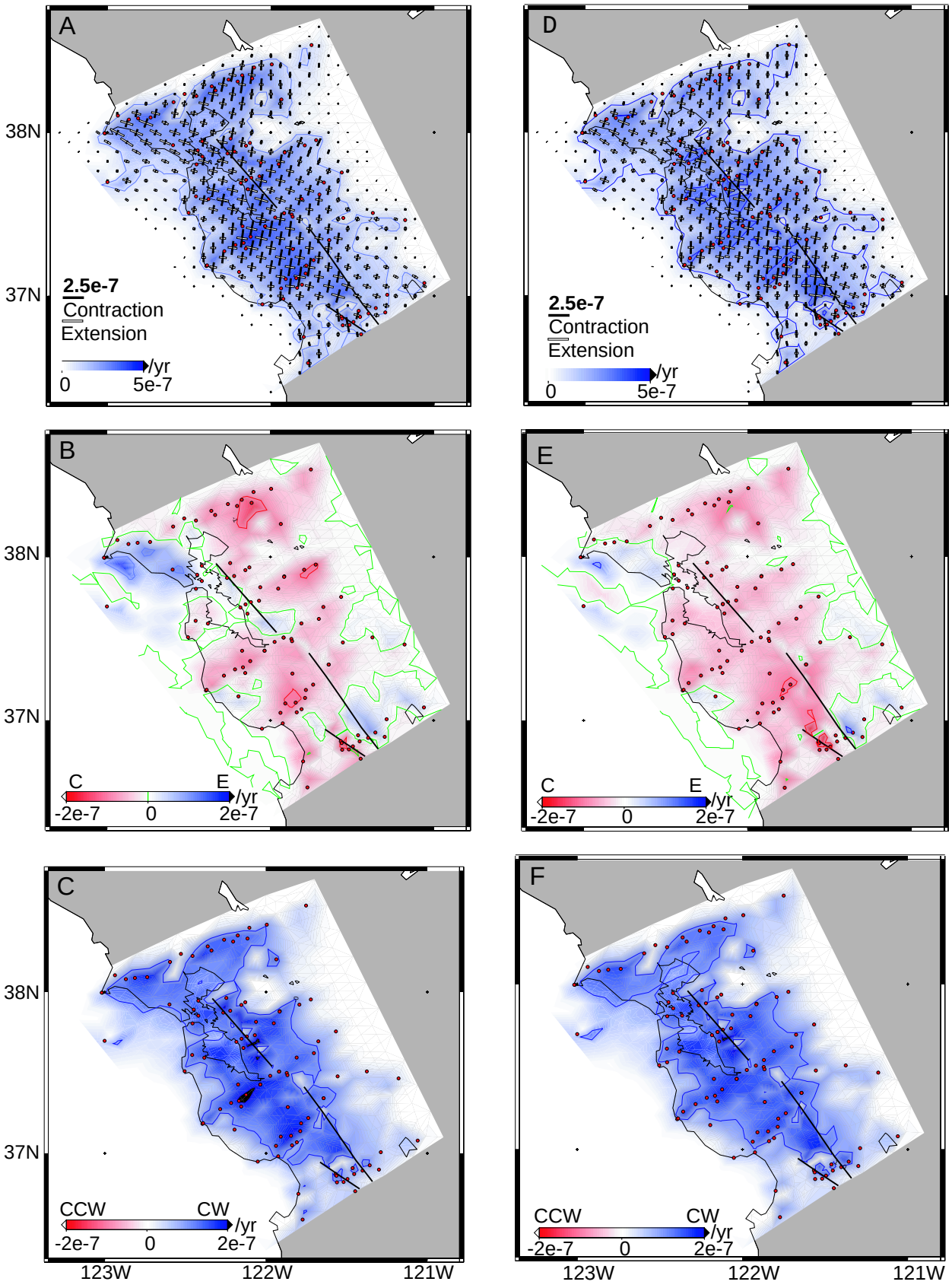
A
D
B
E
C
F
38N
37N
2.5e-7
Contraction
Extension
/yr
0
5e-7
C
E
-2e-7
0
2e-7
CCW
CW
123W
122W
121W

Figure 7

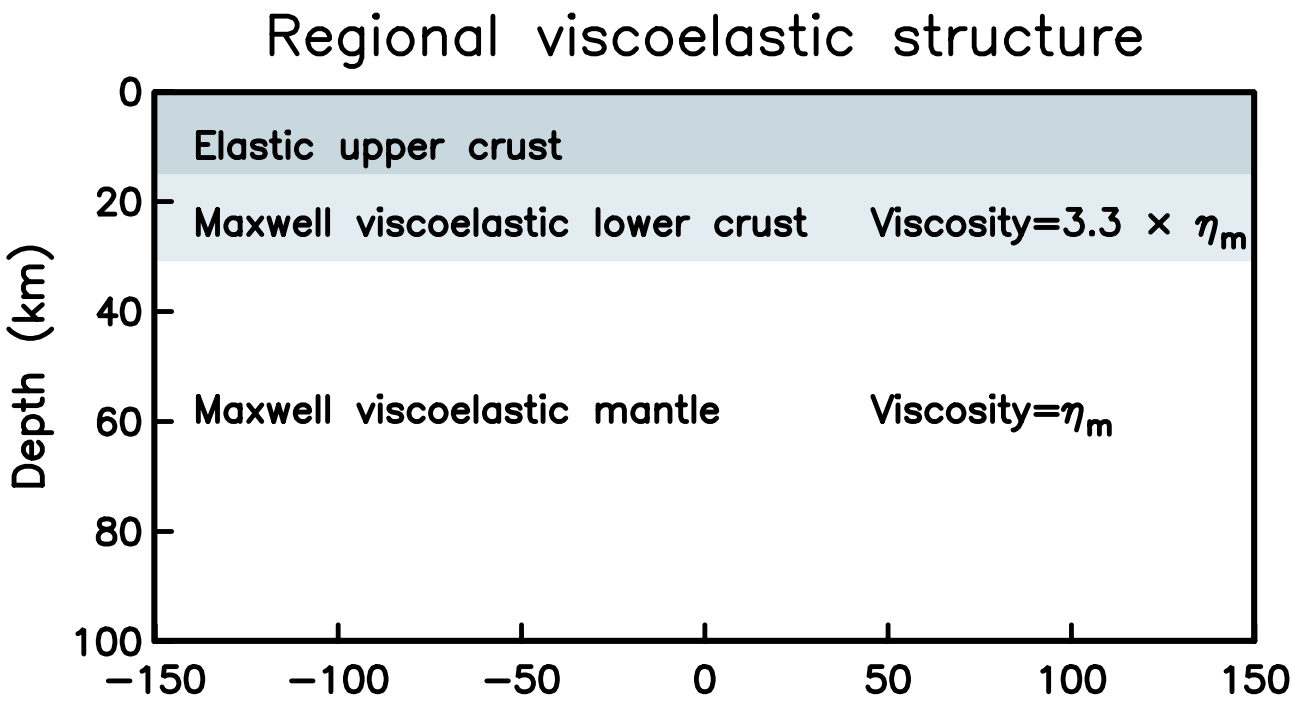
Regional viscoelastic structure
Elastic upper crust
Maxwell viscoelastic lower crust
Viscosity=3.3 × η_m
Maxwell viscoelastic mantle
Viscosity=η_m
Depth (km)
0
20
40
60
80
100
−150
−100
−50
0
50
100
150

Figure 8

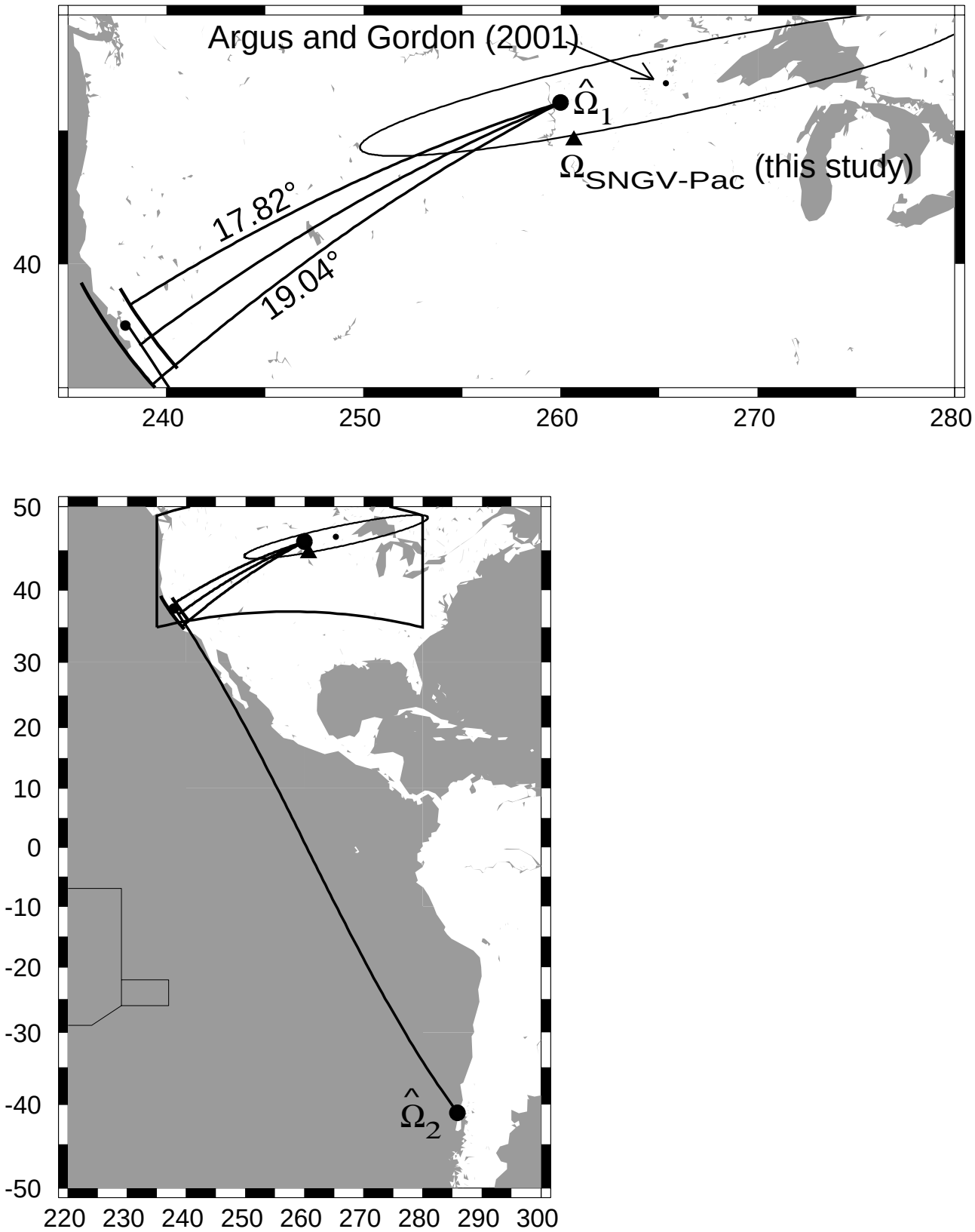
Argus and Gordon (2001)
$\hat{\Omega}_1$
$\Omega_{\text{SNGV-Pac}}$ (this study)
17.82°
19.04°
40
240
250
260
270
280
50
40
30
20
10
0
-10
-20
-30
-40
-50
220
230
240
250
260
270
280
290
300
$\hat{\Omega}_2$

Figure 9

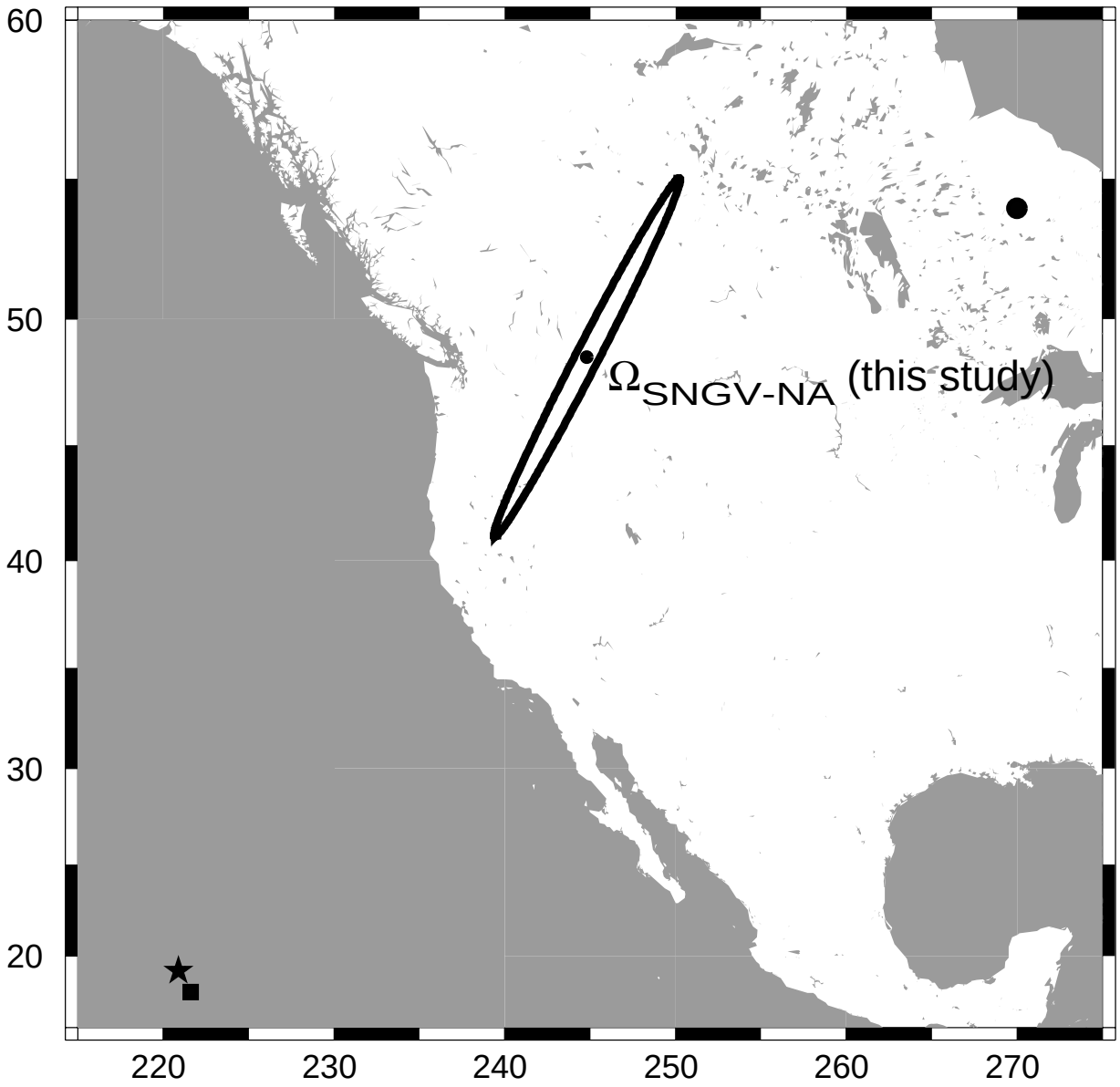
60
50
40
30
20
220
230
240
250
260
270
$\Omega_{SNGV\text{-}NA}$ (this study)

Figure 10

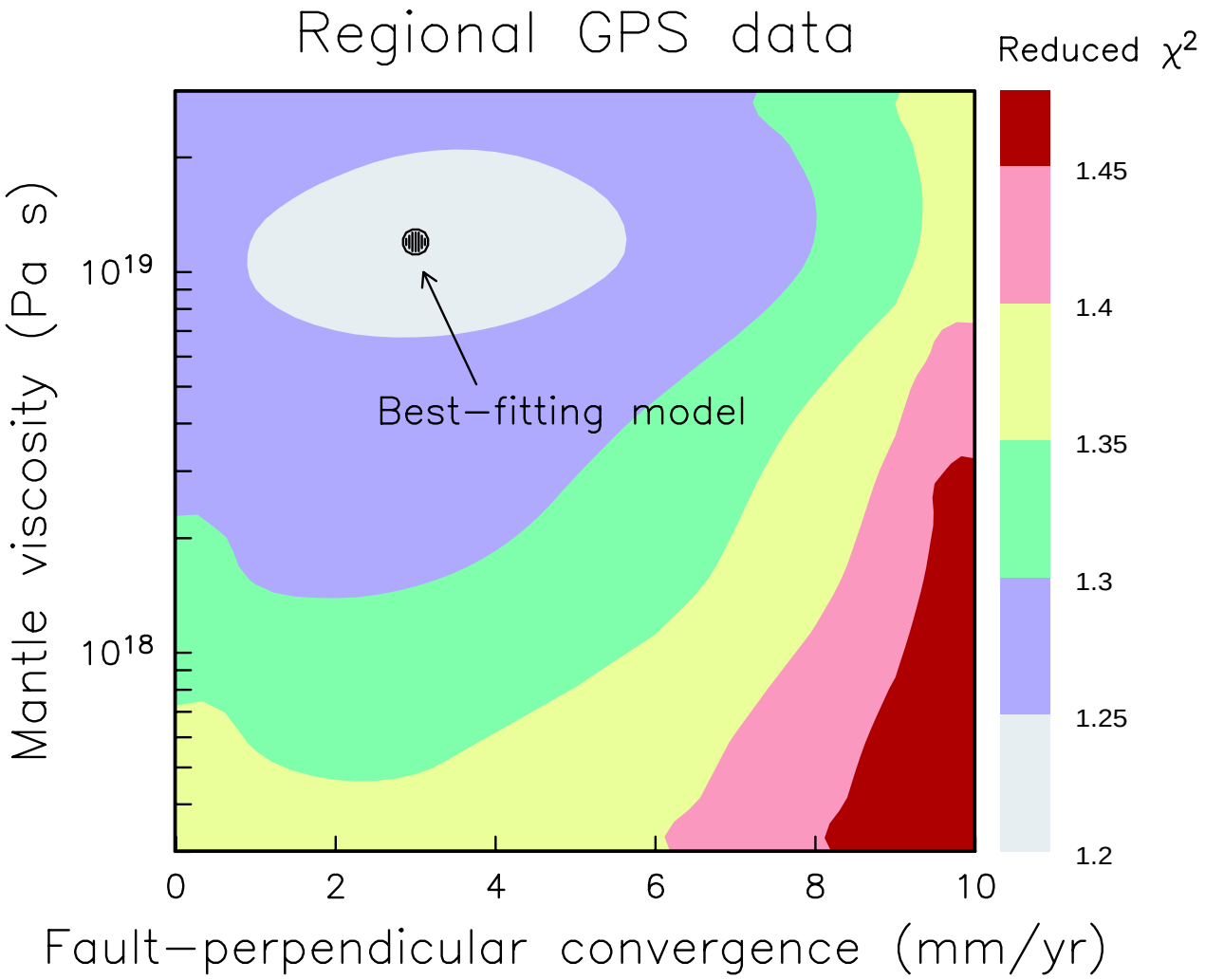
Regional GPS data
Reduced χ^2
1.45
1.4
1.35
1.3
1.25
1.2
Best−fitting model
Mantle viscosity (Pa s)
10^{19}
10^{18}
0
2
4
6
8
10
Fault−perpendicular convergence (mm/yr)

Figure 11

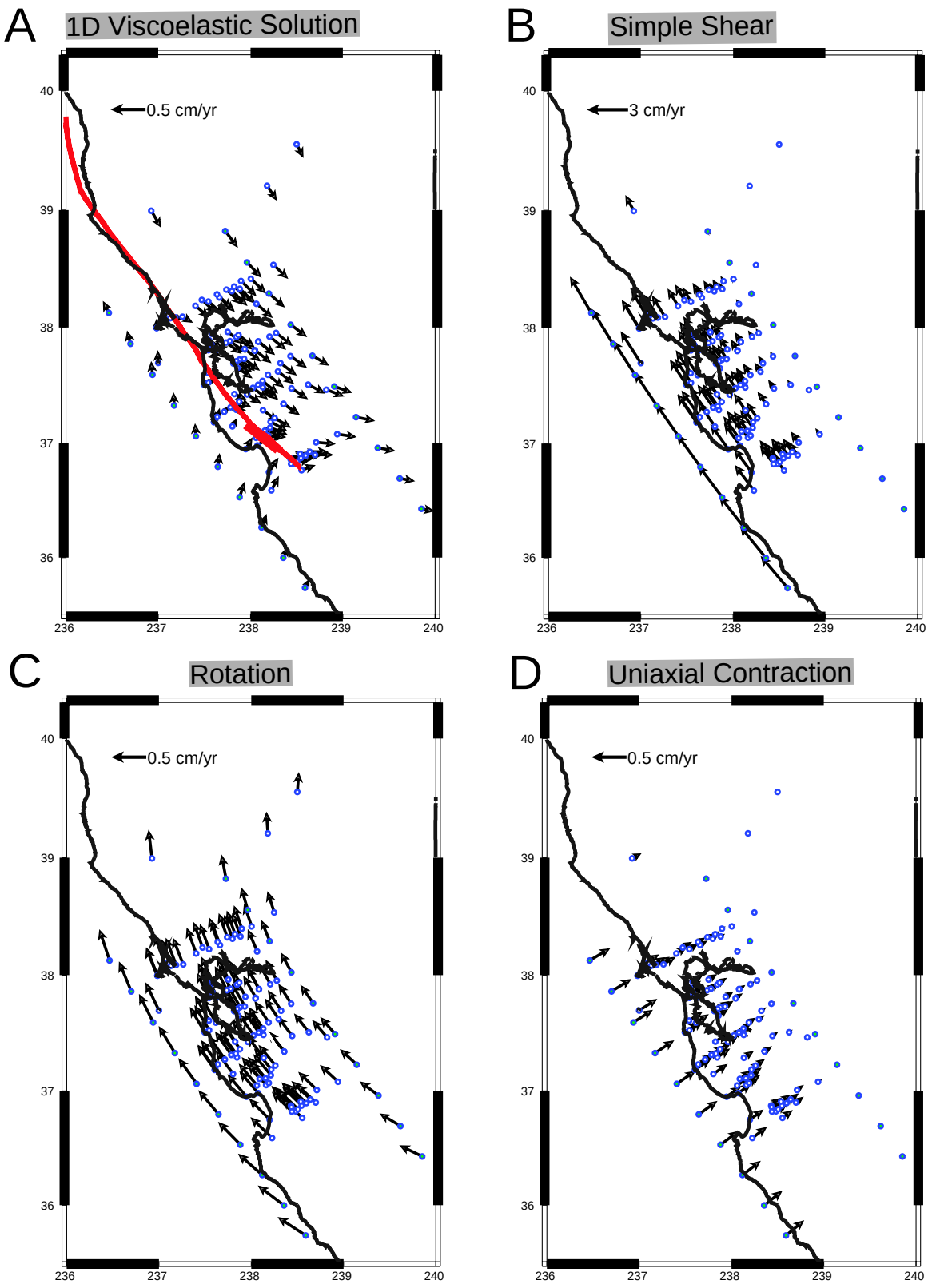
A
1D Viscoelastic Solution
0.5 cm/yr
B
Simple Shear
3 cm/yr
C
Rotation
0.5 cm/yr
D
Uniaxial Contraction
0.5 cm/yr
40
39
38
37
36
236
237
238
239
240

Figure 11

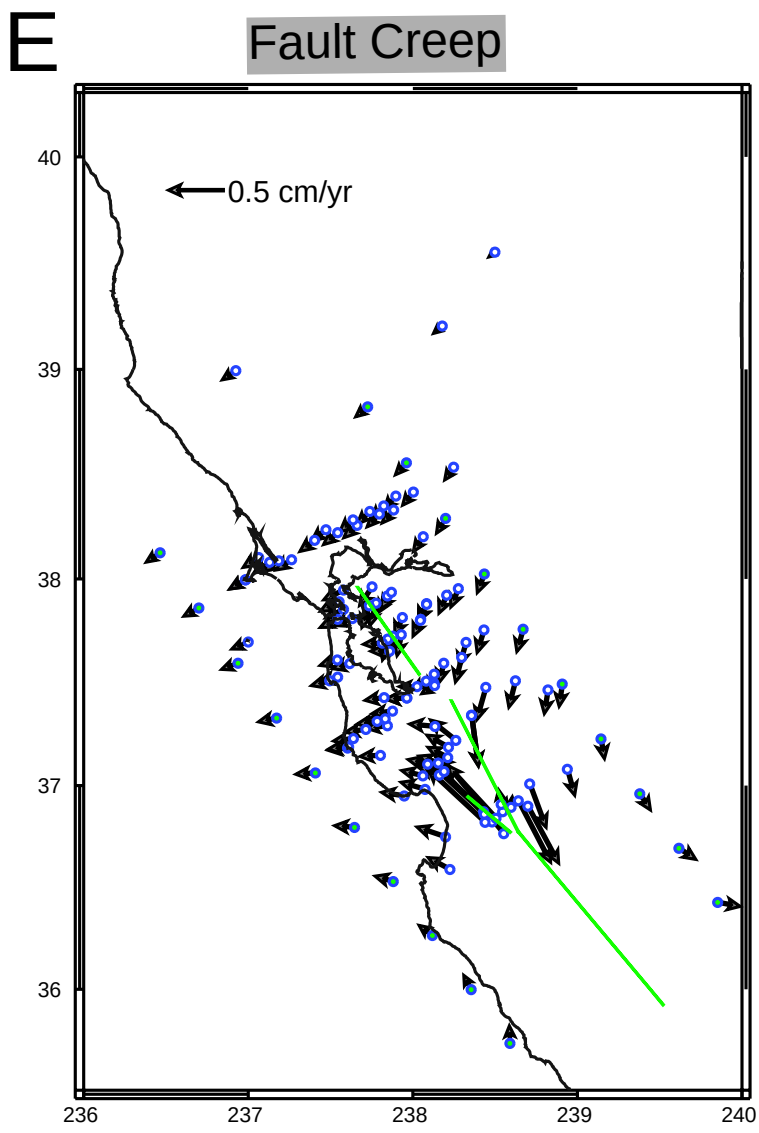

Figure 12

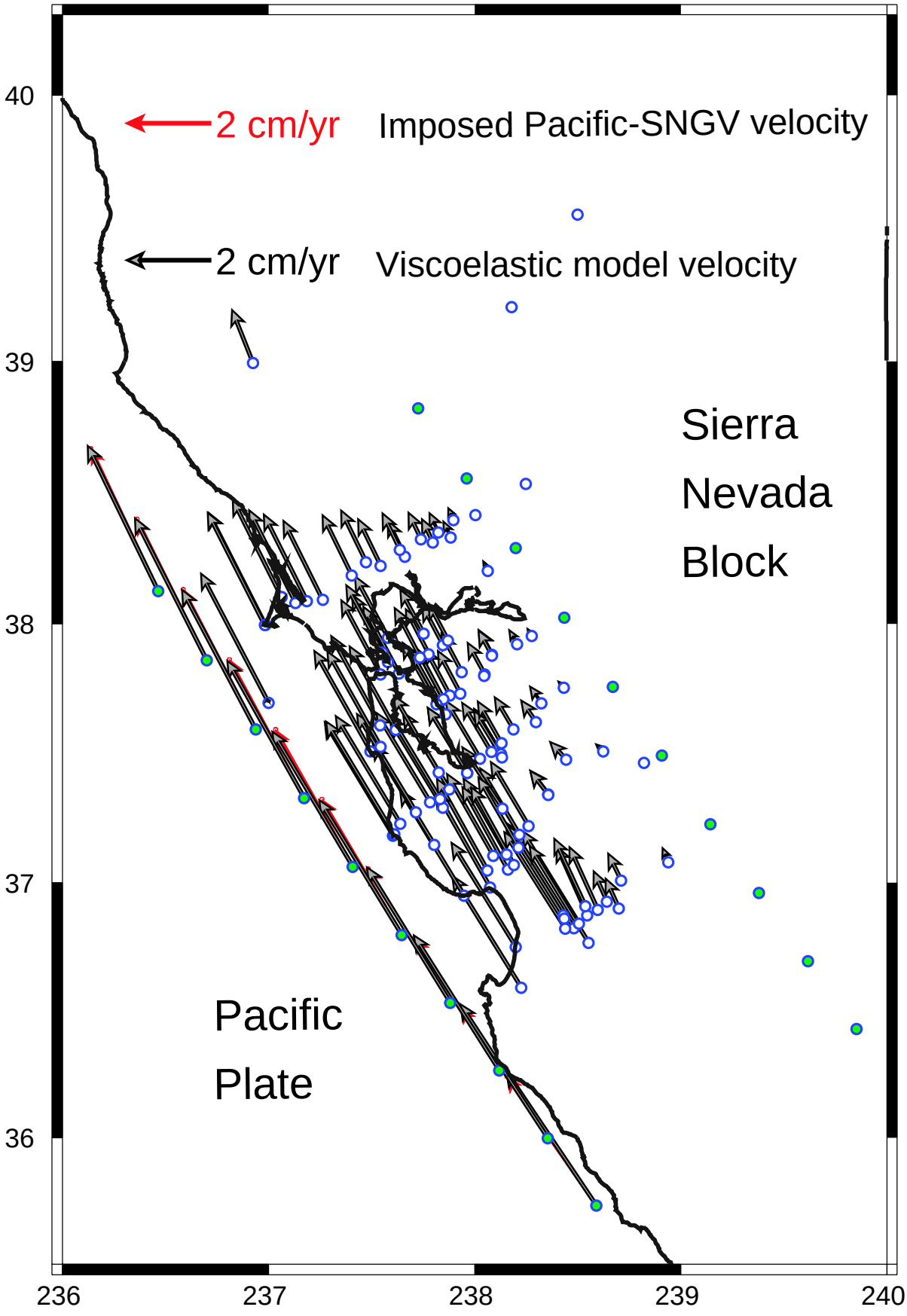
2 cm/yr
Imposed Pacific-SNGV velocity
2 cm/yr
Viscoelastic model velocity
Sierra
Nevada
Block
Pacific
Plate
40
39
38
37
36
236
237
238
239
240

Figure 13

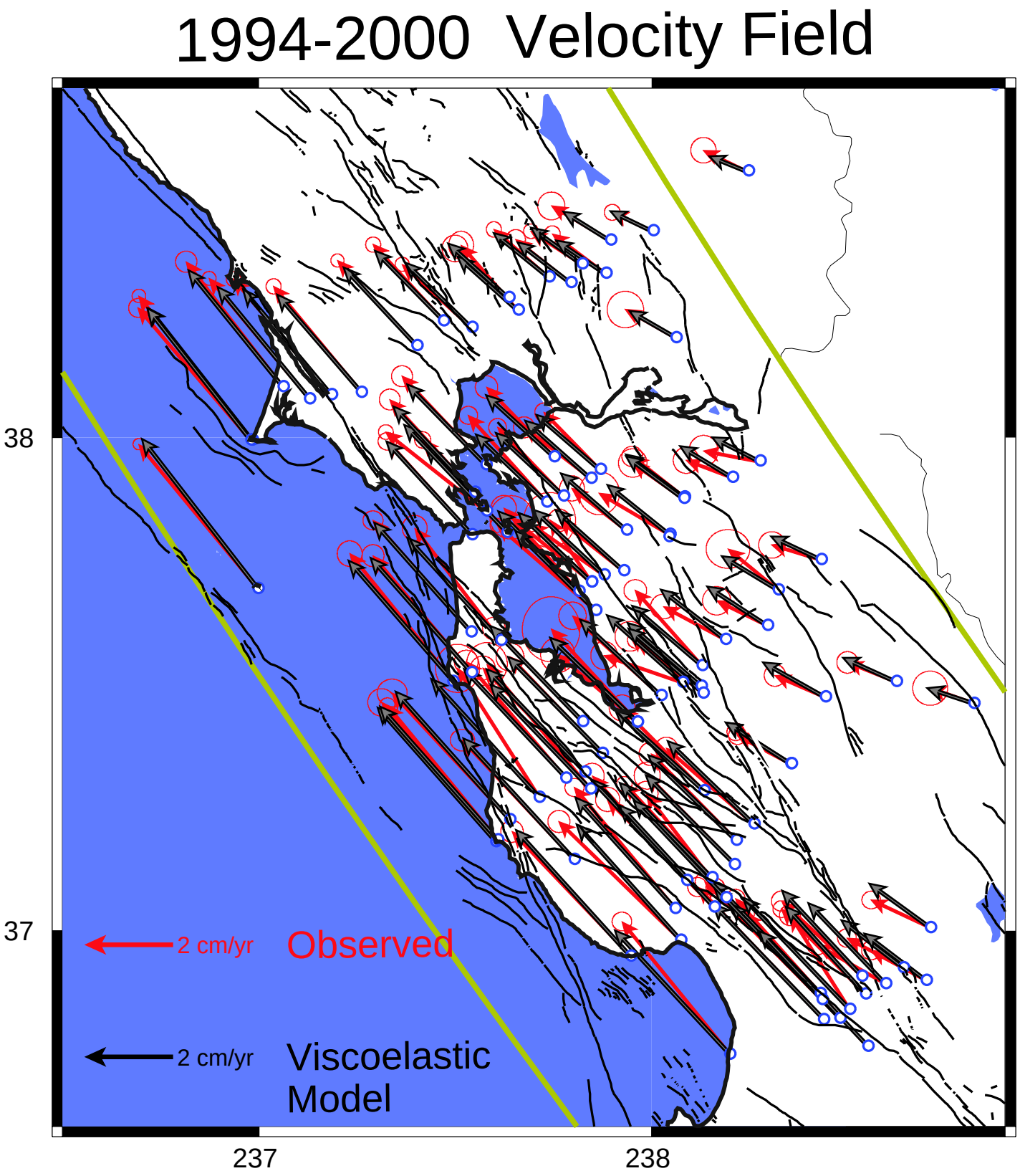
1994-2000 Velocity Field
38
37
237
238
2 cm/yr
Observed
2 cm/yr
Viscoelastic
Model

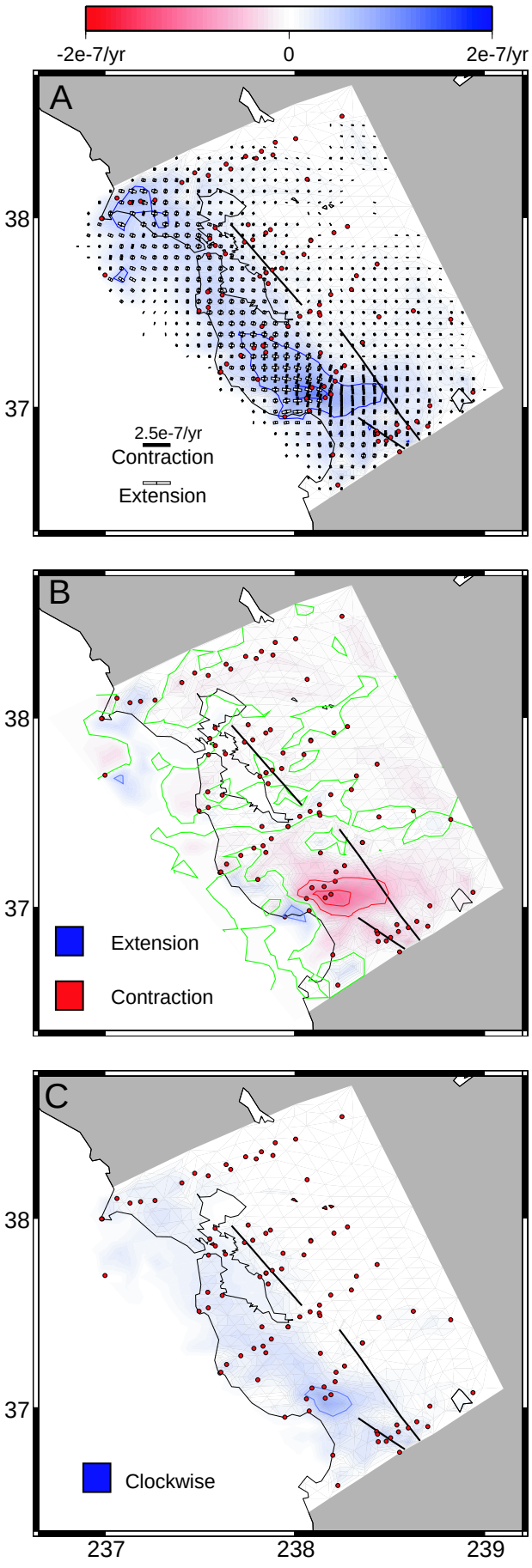
-2e-7/yr
0
2e-7/yr
A
38
37
2.5e-7/yr
Contraction
Extension
B
38
37
Extension
Contraction
C
38
37
Clockwise
237
238
239

Figure 14